J. Fluid Mech. (1999), *vol.* 386, *pp.* 105–126. Printed in the United Kingdom

Axisymmetric propagating vortices in the flow between a stationary and a rotating disk enclosed by a cylinder

By G. GAUTHIER, P. GONDRET AND M. RABAUD

Laboratoire FAST, Bât. 502, Campus Universitaire, F-91405 Orsay Cedex, France

(Received 9 July 1998 and in revised form 30 October 1998)

The destabilization of the stationary basic flow occurring between two disks enclosed by a cylinder is studied experimentally when the radius of the disks is large compared to the spacing. In the explored range of the cell aspect ratio, when one disk only is rotating, circular vortices propagating to the centre are observed above a critical angular velocity. These structures occur naturally but can also be forced by small modulations of the angular velocity of the disk. For each rotation rate the dispersion relation of the instability is experimentally reconstructed from visualizations and it is shown that this dispersion relation can be scaled by the boundary layer thickness measured over the disk at rest. The bifurcation is found to be of supercritical nature. The effect of the forcing amplitude is in favour of a linear convective nature of this instability of the non-parallel inward flow existing above the stationary disk. The most unstable temporal frequency is found to be about four times the frequency of the rotating disk. The evolution of the threshold of this primary instability is described for different aspect ratios of the cell. Finally, two sets of experiments made under transient conditions are presented: one in order to investigate further a possible convective/absolute transition for the instability, and the other to compare with the impulsive spin-down-to-rest experiments of Savas (1983).

1. Introduction

There have been many fundamental experimental and theoretical studies of the flow between rotating disks. Indeed, this is a well-known example of three-dimensional flows and a model geometry to study the cross-flow instabilities and the turbulence that occur in turbomachines. Recently, such a geometry has been used at large Reynolds number to study the statistical properties of turbulence, both numerically by Brachet (1990) and experimentally by Couder, Douady & Brachet (1991) and Fauve, Laroche & Castaing (1993). The fundamental work is due to von Kármán (1921) who showed for one infinite rotating disk that the Navier–Stokes equations can be reduced to a set of four nonlinear ordinary differential equations by a similarity transformation. Then Bödewadt (1940) extended von Kármán's solutions to a rotating fluid over a stationary disk. The most studied geometry thus corresponds to the flow over a rotating disk and it has been shown that the boundary layer can be unstable and undergoes various instability modes. Two of these modes are known as type I (class B) and type II (class A) spirals and have been studied by Gregory, Stuart & Walker (1955), Faller (1963), Faller & Kaylor (1966), Itoh (1984), Wilkinson & Malik (1985) and recently by Jarre, Le Gal & Chauve (1991, 1996*a*, *b*). More recently, Lingwood

has shown both theoretically (Lingwood 1995) and experimentally (Lingwood 1996) that the flow over a rotating disk is first convectively unstable and afterwards exhibits a convective/absolute transition which seems to correspond experimentally to the onset of laminar–turbulent transition.

This single-disk problem has been extended to two infinite disks by Batchelor (1951) with the same similitude transformation that von Kármán (1921) and Bödewadt (1940) used. However, two different types of solutions have been found for this problem: one by Batchelor (1951) with two separated boundary layers close to the disks and a core rotating as a solid body, and another one by Stewartson (1953) with only one boundary layer on the rotating disk. A large number of studies, reviewed by Zandbergen & Dijkstra (1987), have been done to clarify this point. It appears that, independently of any stability argument, the Batchelor solution exists at low Reynolds number while the Stewartson one only exists for larger Reynolds number. Brady & Durlofsky (1987) address numerically the case of finite but large disks. They introduce an end condition for the flow at the periphery as a matching condition between inner and outer inviscid regions. For such shrouded disks in the rotor/stator case, i.e. the one that interests us in the present paper, they found that the flow usually resembles a Batchelor-type solution even if it does not correspond quantitatively to a self-similar solution. The flow between two finite disks has been experimentally studied by Dijkstra & van Heijst (1983) and Sirivat (1991) when one disk is rotating whereas the second one is fixed. They both found spiral patterns of type I and II, similar to the ones observed in the flow over a single rotating disk. Theoretical studies of this flow can be found in San'kov & Smirnov (1991) and also in Hoffman, Busse & Chen (1998) in a related geometry.

Although the Bödewadt flow has been known since 1940, it has been far less studied. This is probably due to the experimental difficulties in creating a fluid in rotation over a stationary disk. Savas (1983, 1987) experimentally and then Lopez & Weidman (1996) and Lopez (1996) both numerically (with an axisymmetric code) and experimentally studied the stability of such a flow in a cylinder tank under the transient condition of an impulsive spin-down-to-rest. They observed first propagating axisymmetric waves and then spirals over the stationary disk. In the rotor/stator case and for experimental steady conditions, the existence of axisymmetric structures have been mentioned in San'kov & Smirnov (1984) and axisymmetric vortices propagating in the Bödewadt layer have been described by Gauthier, Gondret & Rabaud (1996) and in Schouveiler *et al.* (1996, 1999) when the gap between the disks is not too small. Such structures have been also reported numerically (with an axisymmetric code) but at much larger angular velocity by Cousin-Rittemard (1996) and Cousin-Rittemard, Daube & Le Quéré (1998).

The aim of the present study is to characterize the primary instability leading to propagating axisymmetric waves in the flow between a stationary and a rotating disk enclosed by a cylinder. Our experimental set-up allows us to perturb the basic flow in the form of a small periodic modulation or small impulse in the disk velocity. With this external controlled forcing, we have been able to study carefully the influence of noise on the onset and to determine if the bifurcation is subcritical or supercritical and if the instability is convective or absolute. We will see that even though the cell is closed, the system behaves as a non-parallel open flow. In § 2, we present the experimental set-up and the visualization technique of the fluid flow seeded with anisotropic particles. This technique allow us to visualize the boundary layers attached to each disk and their evolution with both the disk velocity and the radius, and to determine which boundary layer is destabilized when the disk velocity is increased

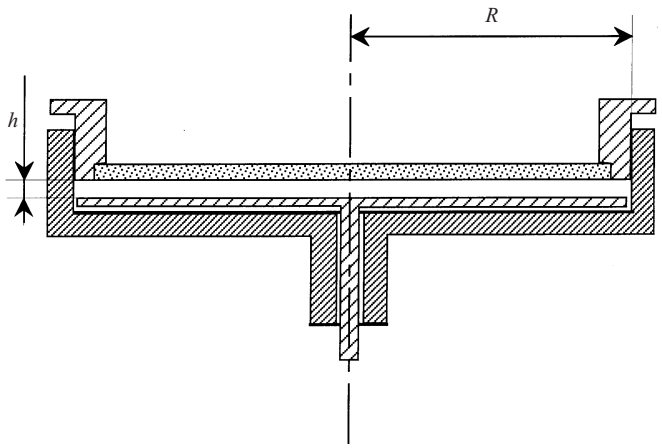

FIGURE 1. Sketch of the experimental set-up. $R = 140\,\text{mm}$ and h is adjustable ($3 < h < 16\,\text{mm}$).

(§ 3). Section 4 is devoted to a general description of the structures observed when no forcing is added. In § 5, we present extensive measurements of the instability obtained with a periodic forcing of the disk velocity, from which, in particular, the dispersion relation is obtained. Finally in § 6 we present some additional transient experiments where the flow response to a small impulse or step and also to spin-down to rest is investigated.

2. Experimental set-up

A section of the cell is presented in figure 1. It consists of a cylinder of small height h closed by a top disk and a bottom disk, both of radius $R = 140\,\text{mm}$. The upper disk is made of glass and is rotating together with the cylindrical sidewall which is made of PVC. The bottom disk is made of rectified brass, coated by a black anodization to improve the visualization contrast. To allow differential rotation the radius of the bottom disk is slightly smaller (a tenth of a millimetre) than the radius of the shrouding cylinder. The thickness h can be adjusted in the range 3 mm to 16 mm by a vertical translation of the top part. Great attention has been paid to the disk parallelism using a set of external wedges. *In situ* measurements show that the thickness h is constant within $\pm 0.07\,\text{mm}$ when the top disk is rotating. As we usually work with h larger than 6 mm, the relative thickness variations are smaller than 1%.

The upper and lateral walls rotate together and the bottom disk can also rotate independently. Each rotation is controlled by a DC motor with a tachometric generator and a regulation loop. After two speed reducers, angular velocity Ω_0 ranging from 0 to $10\,\text{rad s}^{-1}$ with a resolution of $10^{-4}\,\text{rad s}^{-1}$ can be achieved. We have measured the r.m.s. noise intensity in the tachometric signal and found it very low (less than $10^{-4}\,\text{rad s}^{-1}$). The rotation is transmitted to each disk by a belt. When a periodic forcing of the instability is used, a small modulation is added to the command signal. The angular velocity is $\Omega(t) = \Omega_0 + \Delta\Omega \cos \omega t$, with a modulating frequency in the range $10 < \omega < 30\,\text{rad s}^{-1}$. The results presented in this paper correspond to the bottom disk at rest and a rotating top disk; however, the same structures and dynamics are observed in the reverse case despite the fact that our set-up is not completely up/down symmetrical as the cylindrical side wall is attached to the upper disk.

The cell is completely filled with a mixture of glycerol, water and a suspension of anisotropic flakes (by volume 21% of glycerol, 76% of water and 3% of Kalliro-

scope †) so that the viscosity is $\nu = 2.0 \times 10^{-6}$ m^2 s^{-1} at 20 °C. We observe the light reflected by the flakes. As we will see in the figures, the spatial variation of the reflected light gives easily information such as the wavelength or the phase velocity of the structures. In a previous study (Gauthier, Gondret & Rabaud 1998), we have shown that, in three-dimensional flows, this light intensity is not generally due to particles having some static orientation but to particles rotating in a plane that depends on the local velocity gradient tensor of the flow. Quantitative information about the velocity field is not straightforward to extract from the visualization; however, in the particular case of the rotating disk flow, we have shown that the thickness of the boundary layers is proportional to the distance of an observed bright line from a disk. Furthermore, it has been shown that the co- or contra-rotative nature of vortices can be inferred from observation on both sides of a laser sheet as two vortices of opposite sign do not reflect the same light in the same direction. The global or maximum light intensity was shown to be proportional to the particle concentration as long as interactions between the flakes can be neglected; however, the contrast of the images decreases in a few days. The proportionality between the light intensity of bifurcated patterns and the perturbed velocity field remains to be demonstrated, but in the following, we will assume as usual a linear relation for a quantitative study of the instability.

Two visualization techniques allowed us to explore the flow structure. In the first axisymmetric one, the light source is a 40 W circular fluorescent lamp of radius larger than the disks, concentric to the cell and located a few tenths of a centimetre above. A CCD camera is placed on the axis of symmetry about one metre above the set-up in order to observe the entire cell through the upper glass disk. In the second technique, the light source consists of a laser sheet created by an helium-neon laser diode and a cylindrical lens. Usually, the sheet is located in a plane containing the radial and axial directions. In this case another camera with a macro lens is located close to the upper disk and oriented parallel to the bisector between the axial direction and the normal to the laser sheet. The images are digitized on 8 bits and processed with the freeware NIH Image ‡. More details about the set-up can be found in Gauthier (1998).

To get dimensionless numbers to characterize the transitions, one has to choose among several possibilities of scaling since R, h, ν and Ω_0 are relevant parameters, and all the possible Reynolds numbers are encountered in the literature. Since the work of Ekman (1905) the boundary layer between a fluid and a plane rotating at Ω_0 is known to scale as $\delta_0 = (\nu/\Omega_0)^{1/2}$. This is the only length that exists over a single infinite disk. In such a case, the usual dimensionless number is a local Reynolds number defined as the ratio of the local radius r to the thickness δ_0 (Lingwood 1996). In our closed geometry we choose to use the same Reynolds number as Dijkstra & van Heijst (1983) based on the thickness of the cell: $Re = \Omega_0 h^2/\nu$. The second dimensionless number is the aspect ratio of the cell $\Gamma = R/h$. All the results of this paper correspond to $h = 6.7$ mm, thus to $\Gamma = 20.9$, except in §5.6 where $10 < \Gamma < 40$.

3. Boundary layer localization and evolution

In a two-disk flow configuration, two boundary layers can develop close to the disks according to Batchelor's solution. By analogy to the case of a single disk, the boundary layer close to the rotating disk is usually called the Ekman layer,

† Kalliroscope Corporation, 264 Main Street, box 60, Groton, MA 01450, USA.
‡ Internet address : http://rsb.info.nih.gov/NIH-IMAGE/

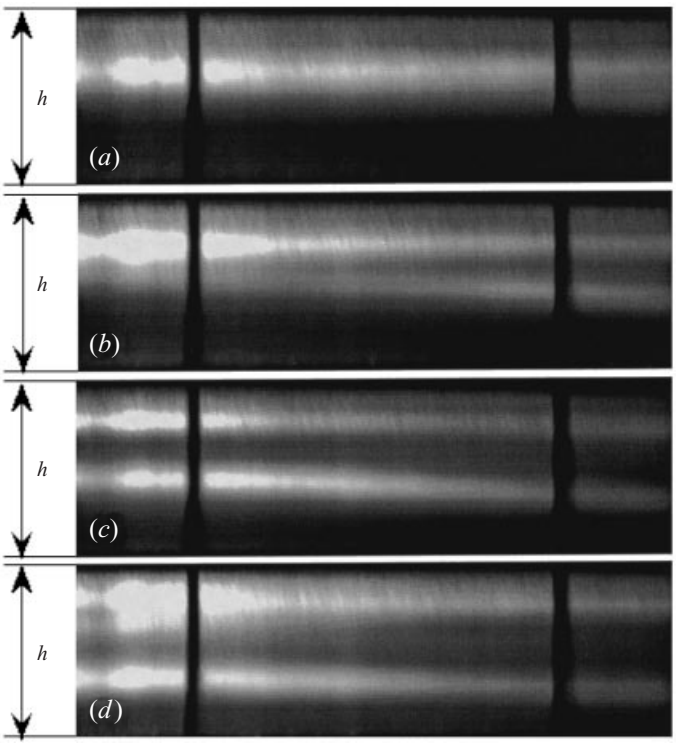

FIGURE 2. Radial laser sheet visualizations for increasing Reynolds number: (*a*) $Re = 44.9$; (*b*) $Re = 61.6$; (*c*) $Re = 91.6$; (*d*) $Re = 145.4$. The image (*d*) is obtained above the threshold of circle appearance but no circle can be seen as it has been time averaged. The two horizontal bright strips in (*b*), (*c*) and (*d*) correspond to the limits of the Ekman (upper) and Bödewadt (lower) boundary layers. In (*a*), these two boundary layers are not yet separated. The two vertical black lines were drawn for measuring purpose and are separated by 13 mm.

whereas the one close to the stationary disk is called the Bödewadt layer. We have determined and measured the thickness of the two boundary layers in our set-up by means of laser sheet visualization. In figure 2 four visualizations of the radial laser sheet perpendicular to the disks are presented for increasing Reynolds number. Above $Re = 52$, two separate thin bright strips related to the two boundary layers are observed. These strips move closer to the disks when the rotation rate increases. At the onset of the instability we observe that the bright line corresponding to the Bödewadt layer undergoes a wavy motion which corresponds to the appearance of circular waves. Following the description of the reflected intensity versus the velocity field for the two-disk flow (Gauthier *et al.* 1998), such visualizations allow us to measure the thickness of the two boundary layers as the distance of these bright lines to the closer disk. To do that, we extract the local extremum of the light intensity at each vertical line of figure 2. The measurements as a function of the radial location and for different Reynolds numbers are reported in figure 3(*a*). Note that no data are obtained near the centre ($r/R < 0.3$), either because our visualization technique is not sensitive enough or because the boundary layers do not exist there, and close to the periphery ($r/R > 0.8$) owing to the size of the camera. As expected, one clearly sees that the thicknesses δ_{Ek} and δ_{Bo} of both layers decrease when the Reynolds number is increased. For a given rotation rate, the Ekman layer remains constant over the radius

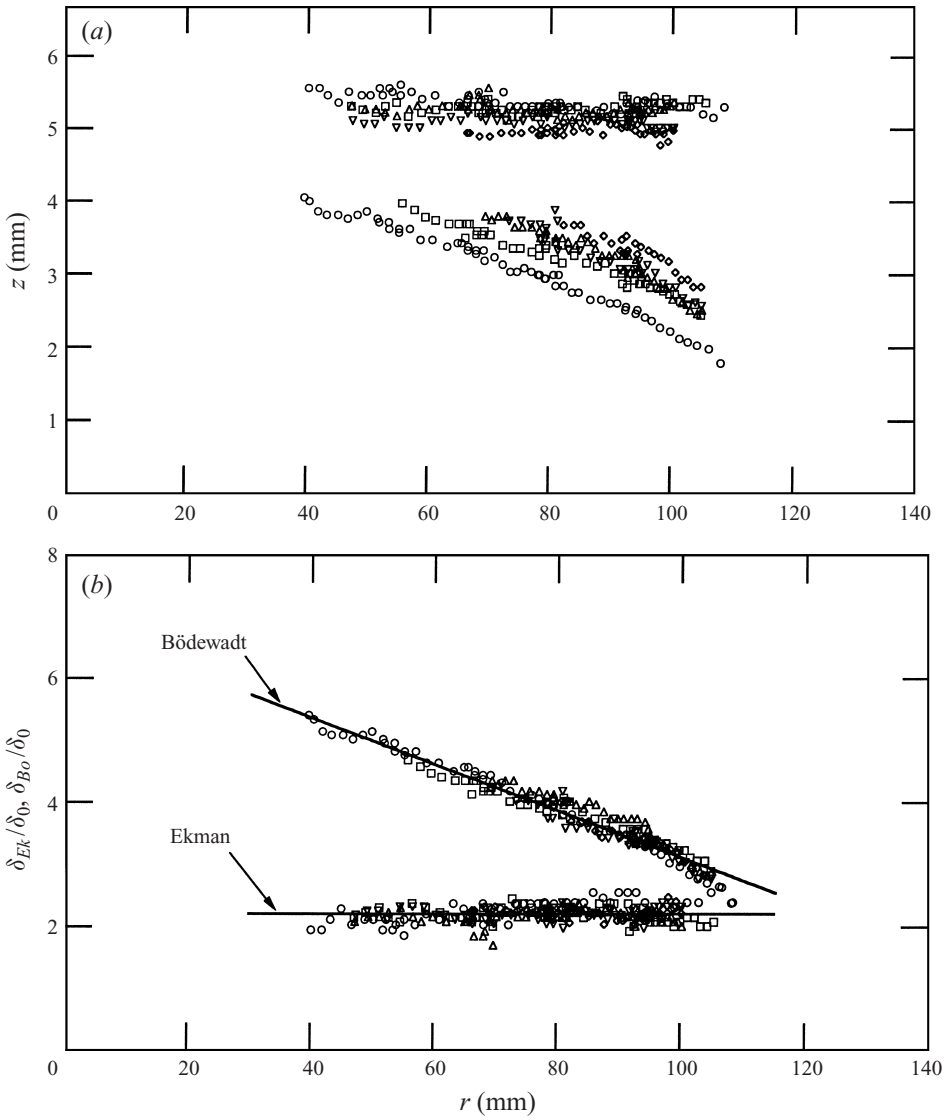

FIGURE 3. (*a*) Position z of the Ekman and Bödewadt boundary layers as a function of the radial position r measured at different Reynolds numbers: $Re = 73.3$ (◇), 84.7 (▽), 103 (△), 107.6 (□) and 130 (○). (*b*) Normalized thicknesses δ_{Bo}/δ_0 and δ_{Ek}/δ_0 of the boundary layers for the same values of Re and a linear fit through the data (—).

whereas the Bödewadt layer increases regularly from the periphery to the centre. By scaling the measurements with the appropriate length $\delta_0 = (\nu/\Omega_0)^{1/2}$, the points collapse onto two curves (figure 3*b*): one of constant value ($\delta_{Ek}/\delta_0 \approx 2.2$) and the other depending on the radius (δ_{Bo}/δ_0). A linear fit gives $\delta_{Bo}/\delta_0 = 6.9-5.3(r/R)$ as the leading-order dependence of the Bödewadt layer on the radius in the middle region of the cell. The Bödewadt layer being larger close to the centre than at the periphery, this suggests that the velocity profiles evolve continuously from a Stewartson one for small r (i.e. only one boundary layer on the rotating disk) to a Batchelor one with a bulk solid rotation for larger r. However, *in situ* measurements will be necessary

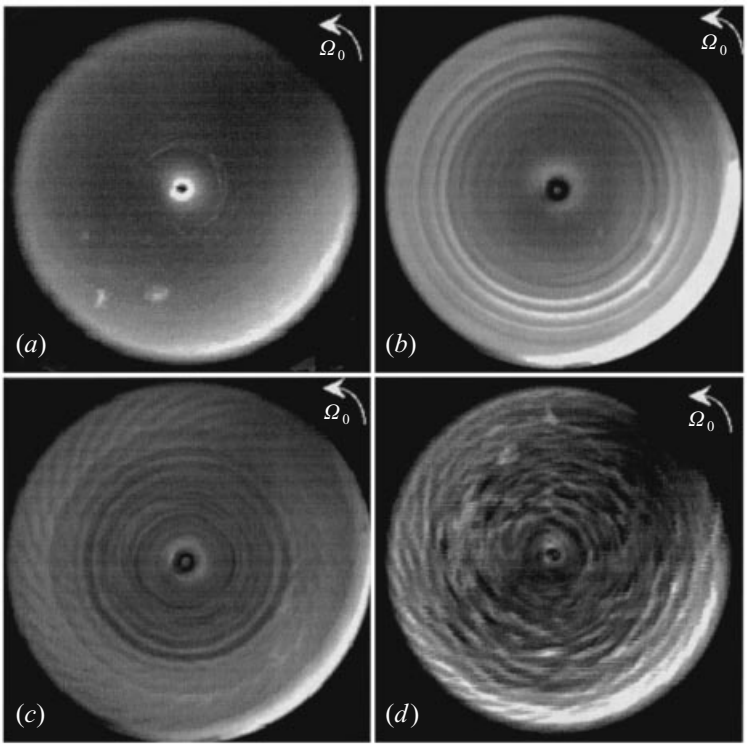

FIGURE 4. Top view image of: (*a*) isotropic reflected light $Re = 40$; (*b*) circles propagating from the periphery to the centre at $Re = 120$; (*c*) spirals (with 31 arms) at the periphery and propagating circles closer to the centre at $Re = 180$; (*d*) disordered state at $Re = 300$. The upper disk is rotating anti-clockwise.

to confirm that point. The rather good collapse of the data observed in figure 3(*b*) shows that δ_0 is the fundamental length scale for the flow but the radial position is also important to describe δ_{Bo}. This radial dependence of the Bödewadt layer is clearly related to the closed geometry, as such dependence is not predicted in the one-disk case (Bödewadt 1940) or in the case of two infinite disks (Batchelor 1951). This radial dependence of the Bödewadt layer has not been clearly mentioned in the literature but can be seen in recent numerical simulations (see figures 5 and 9 of Randriamampianina *et al.* 1997; figure 2 of Lopez 1996 and figure 3*d* of Lopez 1998). This evolution of the flow in the Bödewadt layer suggests that, even if the cell is closed, the flow can have some properties in common with other non-parallel open flows. Indeed, the Bödewadt layer is unstable at larger Reynolds number and structures appear, grow and then decay when advected radially inward in this layer. There is no feedback mechanism induced by the closing of the radial circulation in the outward flow of the Ekman layer, as this layer is stable in the present study. An interpretation in terms of an unstable non-parallel open flow can thus be used and its convective or absolute nature has then to be investigated (Huerre & Monkewitz 1990).

4. Description of the structures observed without forcing

We will now present the patterns observed naturally, i.e. without any added forcing, when increasing the disk velocity and for the aspect ratio $\Gamma = 20.9$. At low rotation

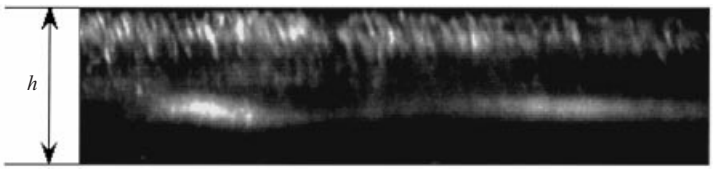

FIGURE 5. Radial laser sheet perpendicular to the disks showing propagating circles at $Re = 120$. The image shows all the height h of the cavity ($h = 6.7$ mm) but only a part of its radial extent (18.7 mm width). Note that the horizontal and vertical scales are not equal. The axis of rotation is located to the left and the top disk is rotating anti-clockwise. Propagating torii appear here as the two bright elongated patches at one third of the height above the bottom disk at rest. These patches propagate to the centre, thus here to the left.

velocities, our visualization from above shows an almost uniform reflected light intensity over the disk (figure 4*a*), in accordance with an axisymmetric and stationary basic flow. Above a critical rotation rate, propagating circular structures corresponding to a spatiotemporal modulation of the reflected light intensity are observed (figure 4*b*). These circular waves, which we will call circles, appear close to the periphery, propagate toward the centre and disappear at a given radius. Note that the threshold for the circle appearance depends on the noise level. With previous less regulated motors, the threshold was found to be $Re \approx 70$ while with the motors now used this threshold is found to be $Re \approx 110$. On increasing the angular velocity, the circles are more distinct and propagate farther toward the centre. At even higher angular velocities, spirals appear at the periphery and circles are then only observed closer to the centre (figure 4*c*). Note that now the onset of the appearance of the spirals does not appear to be sensitive to the noise level. Increasing the angular velocity still further, the spirals progressively invade the cell, and then a disordered pattern corresponding to the onset of turbulence is observed at the centre (figure 4*d*). The circles are thus observed only in a small range of the control parameter. The spirals exhibit typically 30 arms and roll up in the direction of Ω_0 (figure 4*c*), thus corresponding to type II spirals (Sirivat 1991; Schouveiler, Le Gal & Chauve 1998). When using the laser sheet visualization (figure 5), the circular vortices appear as bright patches propagating above the bottom stationary disk. The centres of these patches propagate toward the axis along a trajectory that coincides with the previously observed bright line corresponding to the limit of the Bödewadt layer. Above these patches, we can see a bright thick line corresponding to the still stable Ekman layer. From an observation of the other side of the laser sheet and following the analysis of Gauthier *et al.* (1998), we can conclude that these propagating vortices are co-rotating. The typical wavelength of the circular waves is $\lambda \approx 15$ mm. As the gap thickness is smaller ($h = 6.7$ mm), the vortices have an elongated section. Figure 6 shows a spatiotemporal image of the propagating circular waves at $Re = 128$. This image is built by plotting at successive times a radial video line taken from above. In this figure, the structures can be seen propagating between $r \approx 120$ mm and $r \approx 60$ mm as a succession of bright and dark lines. Even though the pattern is not perfectly regular, we do not see any dislocation: contrary to Cousin-Rittemard *et al.* (1998) and Schouveiler *et al.* (1999), we do not observe any pairing of circular waves during their radial propagation. From the curvature of these lines, one can deduce that the phase velocity of the waves decreases during their motion to the centre.

In summary, only circles can be observed for $70 < Re < 140$, and together with spirals for $140 < Re < 200$. Turbulence appears progressively at the centre with spirals at the periphery when $Re > 200$. In the rest of the paper, we will focus on the

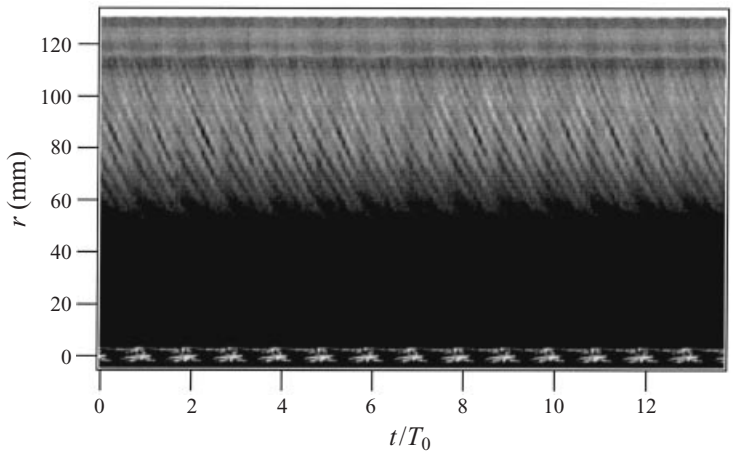

FIGURE 6. Spatiotemporal image of propagating circles observed without forcing at $Re = 128$. This picture is constructed by plotting at successive times ($\Delta t \approx 1/17$ s) a single video line of a picture taken from above (radial line of images like the one of figure 4*b*). The time t is normalized by the period of rotation of the disk $T_0 = 2\pi/\Omega_0$.

circular waves and, as we have seen that their appearance seems to depend strongly on the noise level, we will study the flow response to some external controlled excitation.

5. Flow response to a periodic forcing

In order to characterize quantitatively the circular waves, we impose an external forcing by modulating the angular velocity Ω_0 of the rotating disk. The angular velocity is now $\Omega(t) = \Omega_0 + \Delta\Omega \cos \omega t$. This forcing is applied to all the disk and so is non-local. Most of the results presented hereafter will correspond to $\Omega_0 = 5.25$ rad s^{-1} and $\Gamma = 20.9$ ($Re = 120$), and to a modulation of amplitude $\Delta\Omega/\Omega_0 = 6.5\%$. Similar results are found if the modulation is imposed on the stationary disk.

5.1. *Spatial amplitude of the reflected light*

Figure 7(*a*) shows a spatiotemporal image of the propagating circular waves when excited. Figure 7(*b*) corresponds to a time filtering of figure 7(*a*) consisting of a narrow band-pass filter centred on the forcing frequency. The narrow filtering is justified here when one looks at the temporal power spectrum density (PSD) of the light intensity signal at one point (figure 8). The peak ω corresponding to the circles is sharp and by far the strongest compared to the other peaks, which correspond mainly to the rotation frequency Ω_0 and its harmonics. Note that these frequencies may appear either because the set-up is not perfect and triggers some perturbations in the flow, or because the optical transmission through the upper glass disk is non-constant around the perimeter. Since the time frequency at each radial position remains equal to the forcing frequency ω and as the bright lines in the spatiotemporal images of figure 7 are curved showing that the phase velocity decreases toward the centre, one can deduce that the wavenumber increases continuously toward the centre.

The intensity $I(r,t)$ along each radial video line (any vertical lines of figure 7) is $I(r,t) = I_0(r)\cos(\int k_r(r)\,\mathrm{d}r - \omega t)$, where $k_r(r)$ is the local wavenumber and $I_0(r)$ the amplitude of the light modulation. The local amplitude $I_0(r)$ increases and then decreases from the periphery toward the centre, with a maximum I_{max} at a given

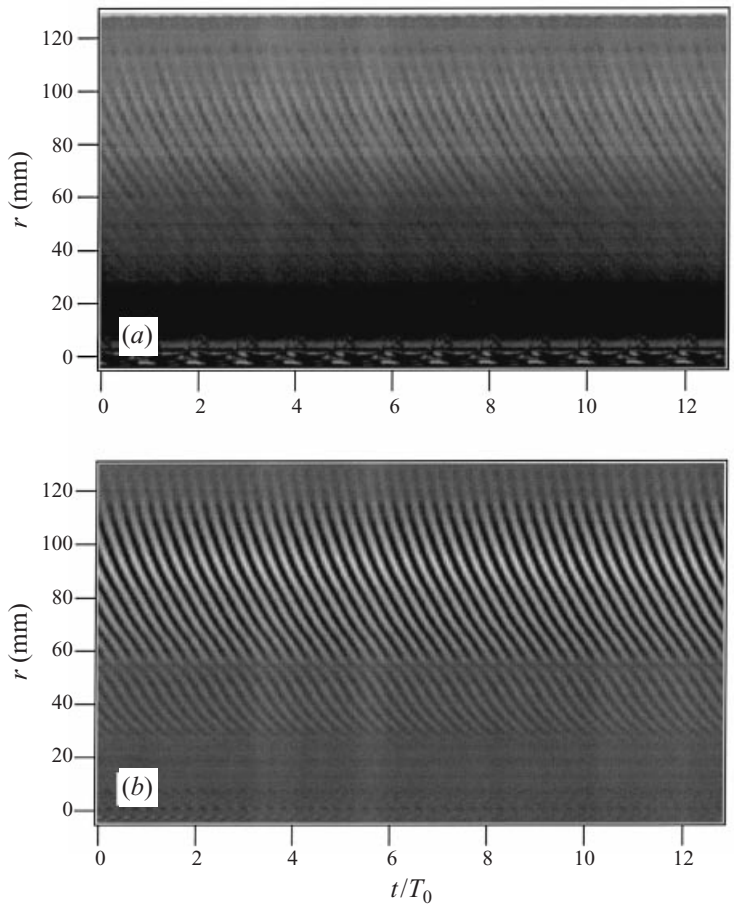

FIGURE 7. Non-filtered (*a*) and filtered (*b*) spatiotemporal image of propagating circles observed at $Re = 120$ and with a periodic forcing corresponding to $\omega = 18.84\,\mathrm{rad\,s^{-1}}$ and $\Delta\Omega/\Omega_0 = 6.5\,\%$.

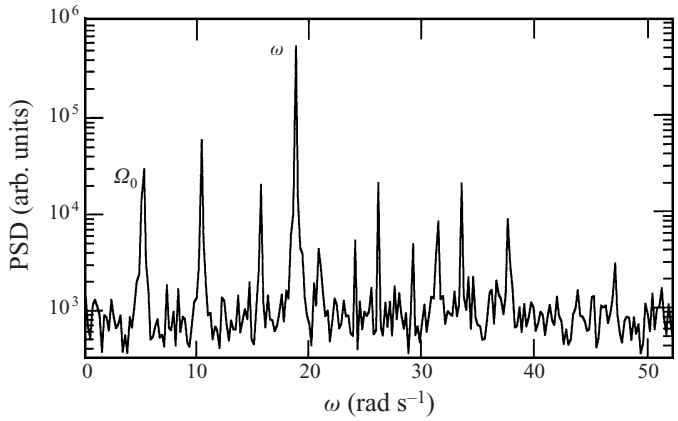

FIGURE 8. Power spectrum density (PSD) of the non-filtered time signal of the light intensity at one point ($r = 114\,\mathrm{mm}$ in figure 7*a*): $\Omega_0 = 5.25\,\mathrm{rad\,s^{-1}}$ ($Re = 120$), $\Delta\Omega/\Omega_0 = 6.5\%$ and $\omega = 18.84\,\mathrm{rad\,s^{-1}}$. The frequency of rotation and its harmonics are visible but one order of magnitude less than the response to the forcing at ω.

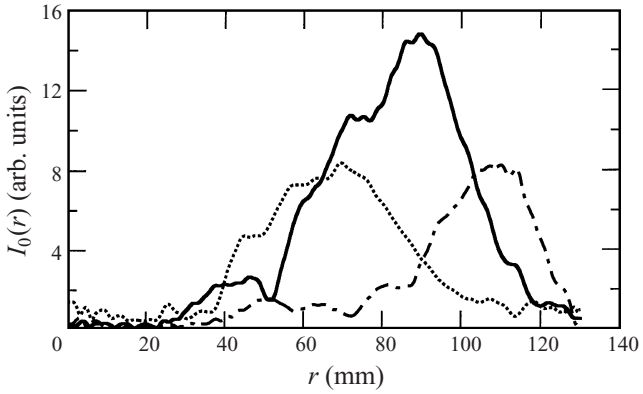

FIGURE 9. Light intensity I_0 as a function of the radial position r at $Re = 120$ and for different forcing frequency: $\omega = 10$ (- - -), 17.6 (—) and 30.2 rad s^{-1} (— - —).

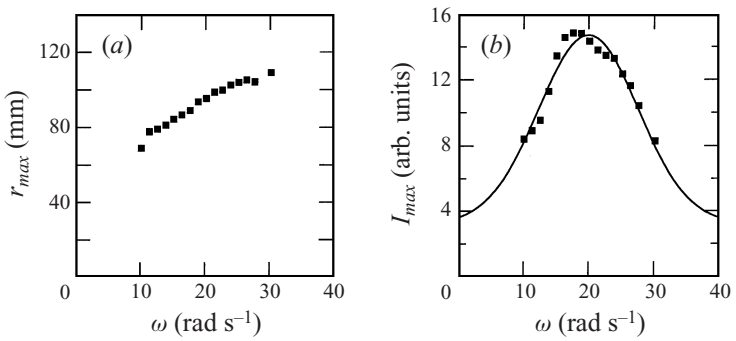

FIGURE 10. (*a*) Evolution of r_{max} as a function of the forcing angular frequency ω at $Re = 120$ ($\Omega_0 = 5.25$ rad s^{-1}). (*b*) Maximum light intensity I_{max} versus ω: experimental data (■) and best fit by a Gaussian curve (—) of resonance frequency 20 rad s^{-1} and standard deviation 11 rad s^{-1}.

radius r_{max} (figure 9). The radius r_{max} increases almost linearly when the forcing frequency increases (figure 10*a*) whereas I_{max} exhibits the shape of a resonance curve (figure 10*b*). This resonance curve being wide (the factor of quality is of order one), the flow is a rather large-band amplifier, with a most amplified frequency which is around four times the disk frequency Ω_0. Note that such a spatial variation of the amplitude of the waves of figure 9 (initial growth followed by decay) is classical for an unstable non-parallel flow.

5.2. *Local wavenumber and spatial growth rate of the circular waves*

In our closed cell there is a general circulation (outward in the Ekman layer and inward in the Bödewadt one) and the instability appears only in part of the Bödewadt layer. As this layer is of increasing thickness, the flow is a spatially developing one. Thus the instability behaves like one of an open flow and we will now use a spatial description (Huerre & Monkewitz 1990). In spatial normal mode analysis, the permanent perturbed velocity field is proportional to $\exp[\mathrm{i}(\int k\ \mathrm{d}r - \omega t)]$ with real constant ω and complex wavenumber $k = k_r + \mathrm{i}k_i$. The real part k_r is the local wavenumber of the pattern and k_i is the spatial growth rate in the propagating direction (inward).

The local wavenumber $k_r(r)$ is extracted from the light intensity along a radial line

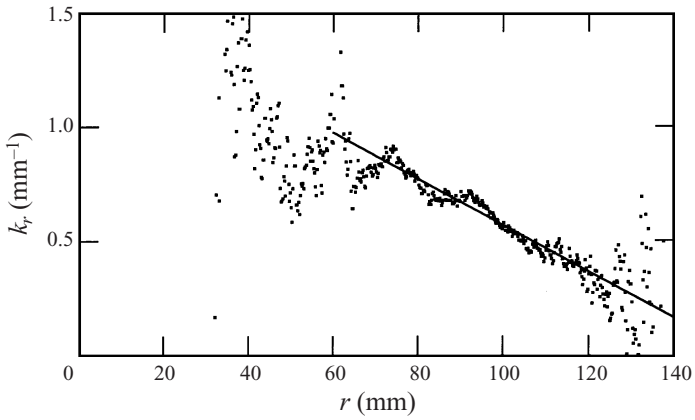

FIGURE 11. Wavenumber k_r as a function of the radial position r at $Re = 120$ and $\omega = 18.8$ rad s^{-1} measured at the different times of figure 7. The continuous line $k_r = 1.59 - 0.01r$ is a linear fit through the data. The dispersion of the data is due to a very low signal for large or small r.

(e.g. any vertical line of figure 7*b*) through a demodulation process using a Hilbert transformation (Croquette & Williams 1989). Figure 11 represents the wavenumber k_r as a function of the radius r for one forcing frequency ω and shows that, when the structures are clearly observed, k_r increases almost linearly when r decreases. The same data are extracted for various forcing frequencies and the dispersion relation $(k_r(r), \omega)$ at different selected radial positions is plotted in figure 12(*a*). The curves corresponding to different radial positions are roughly linear and with a constant slope $\partial\omega/\partial k_r \sim 30$ mm s^{-1} whatever the radius. The phase velocity $v_\phi = \omega/k_r$ increases weakly with ω for small r but decreases more significantly with ω for large r, being nearly constant for $r = 80$ mm.

The local spatial growth rate $k_i(r)$ is also extracted from the light intensity curves $I_0(r)$ of figure 9 using a WKBJ approximation (Hinch 1991), i.e. assuming locally an exponential growth of the light intensity: $\mathrm{d}I_0/\mathrm{d}r = -k_i(r)I_0$. Such a WKBJ approximation requires a weakly non-parallel flow, i.e. in our case that the spatial evolution of the boundary layer is small on the scale of a wavelength. Figure 3 shows that for $\lambda \approx 15$ mm, the relative evolution of the Bödewadt layer is less than 10%. As the waves propagate from the periphery to the centre they are first amplified ($k_i(r) > 0$ for $r > r_{max}$) then marginal ($k_i(r) = 0$ for $r = r_{max}$) and finally damped ($k_i(r) < 0$ for $r < r_{max}$). Figure 12(*b*) shows the evolution of $k_i(r)$ versus ω for different radial positions. Such a figure only shows that, at each frequency, the spatial growth rate is either negative or positive depending on the radius. The representation $(k_i(r), k_r(r))$ of figure 13(*a*) seems to be a better one. Despite some scattering in the data, the growth rate is positive for a band of unstable wavenumbers, roughly between 0.1 and 0.6 mm^{-1}, and negative for higher stable wavenumbers. The scattering of the data can be strongly reduced when using $k_r(r)$ and $k_i(r)$ multiplied by the thickness $\delta_{Bo}(r)$ of the Bödewadt layer which is the physical length of the flow at radius r (figure 13*b*). Note that with a local analysis using the local Reynolds number defined as the ratio r/δ_0 or r/δ_{Bo}, the data do not collapse so clearly on a single curve. Figure 13(*b*) shows that the locally most unstable wavenumber is $k_{r_{max}} \approx 0.5/\delta_{Bo}$ whatever the position and the forcing frequency. The marginal wavenumber which corresponds to the brightest circles is of the order of $1.5/\delta_{Bo}$, thus three times larger than the most unstable one. Note that our experimental value of $k_{r_{max}}$ is similar to the one found theoretically by

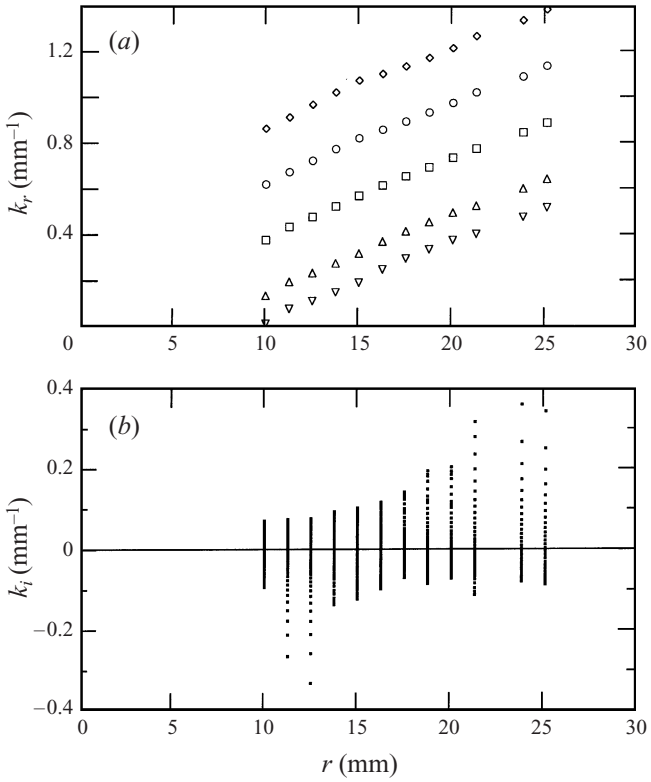

FIGURE 12. (*a*) Local wavenumber k_r as a function of the forcing frequency ω at $Re = 120$ for five different radial positions: $r = 34$ (◇), 57 (○), 80 (□), 102 (△) and 114 mm (▽). (*b*) Spatial growth rate k_i versus ω for fifty different radial positions ($34 < r < 128$ mm).

Lingwood (1997) ($k_{r_{max}} \approx 0.33/\delta_0$) at the convective/absolute transition in the case of propagating circular waves in the Bödewadt flow above a single infinite disk.

5.3. *Influence of the Reynolds number*

All the results presented above were obtained for a given angular velocity Ω_0 and a gap spacing h, hence for a given Reynolds number Re. We will now investigate the effects of changing the Reynolds number by changing Ω_0. Figure 14(*a*) shows the evolution of the maximum dimensionless growth rate $k_{i_{max}}\delta_{Bo}$ as a function of the Reynolds number. For a supercritical instability the growth rate is known to increase linearly above threshold. A linear fit through our data gives a rough estimation for the threshold Re_c of the instability: $Re_c = 65 \pm 10$. Note that whatever the Reynolds number, we find that the most unstable wavenumber always corresponds to $k_{r_{max}} \approx 0.5/\delta_{Bo}$, suggesting that the critical wavenumber at Re_c is non-zero and equal to this value. Similarly, we plot the square of the width of the range of unstable wavenumbers $[\Delta(k_r\delta_{Bo})]^2$ versus Re (figure 14*b*). Again, a linear fit suggested by a supercritical bifurcation gives a critical Reynolds number $Re_c \approx 82 \pm 8$. This fit through the data allows us to determine the curvature of the marginal stability curve which is the coefficient ξ_0 of the diffusive term in an underlying Ginzburg–Landau equation (Jarre *et al.* 1996*b*). We find that $\xi_0/\delta_{Bo} \approx 8$.

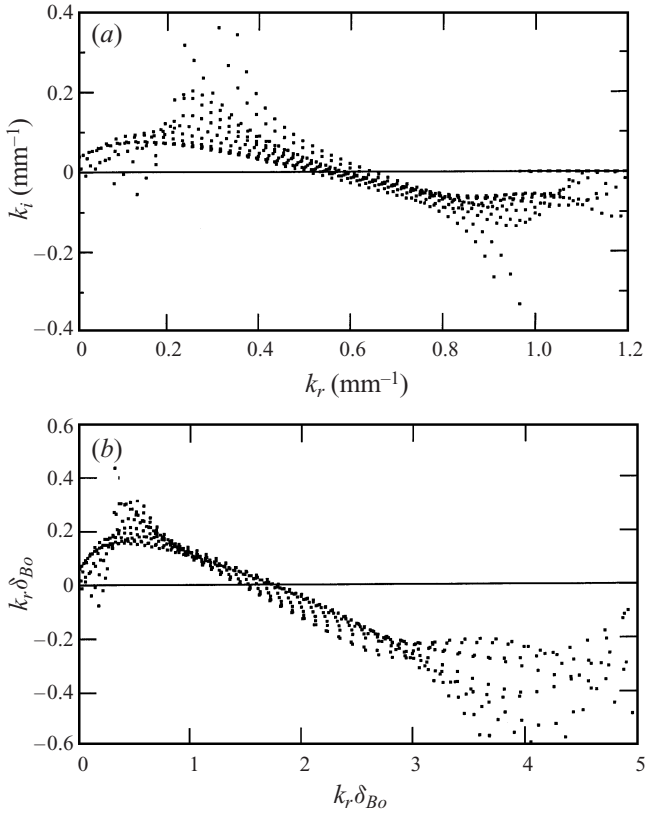

FIGURE 13. (*a*) Spatial growth rate k_i versus the local wavenumber k_r at $Re = 120$ for different radial positions ($34 < r < 128$ mm). (*b*) Normalized spatial growth rate $k_i(r)\delta_{Bo}(r)$ as a function of the normalized local wavenumber $k_r(r)\delta_{Bo}(r)$ at $Re = 120$ for different forcing frequencies ($10 < \omega < 25$ rad s^{-1}) and radial positions ($34 < r < 128$ mm).

5.4. *Influence of the noise level*

To determine a possible effect of the noise level on the apparent threshold of the instability, we have tested various forcing amplitudes. In figure 15(*a*) the maximum observed light intensity I_{max} of the circular structures is plotted versus Re for four different forcing amplitudes $\Delta\Omega$ but at a given forcing frequency ω. The light intensity I_{max} exhibits a sharp increase when Re increases. Furthermore at a given Re, I_{max} appears to increase with the forcing amplitude $\Delta\Omega$. To test the linear dependence of I_{max} upon $\Delta\Omega$, we plot the ratio $I_{max}/\Delta\Omega$ versus Re in figure 15(*b*). The collapse of the data on a single curve for $Re < 110$ shows that the response I_{max} doubles when doubling $\Delta\Omega$. This result demonstrates that, even at large forcing amplitude, we are still in the linear regime of a supercritical instability. From this figure the threshold of the instability, determined as the inflection point of the curve, appears to be around $Re \approx 70 \pm 5$.

It is worth recalling that without controlled forcing we do not observe any structures until $Re > 110$. We believe that this result is not in contradiction with a supercritical instability. Indeed the forcing imposed in figure 15 corresponds for e.g. $\Omega_0 = 3$ rad s^{-1} ($Re = 67$) to $\Delta\Omega/\Omega_0 = 0.16, 0.11, 0.04$ and 0.004. When no forcing is added, the natural mechanical noise corresponds to $\Delta\Omega/\Omega_0 = 4 \times 10^{-5}$, as estimated from the r.m.s. signal given by the tachometric generator of the motor in the frequency range

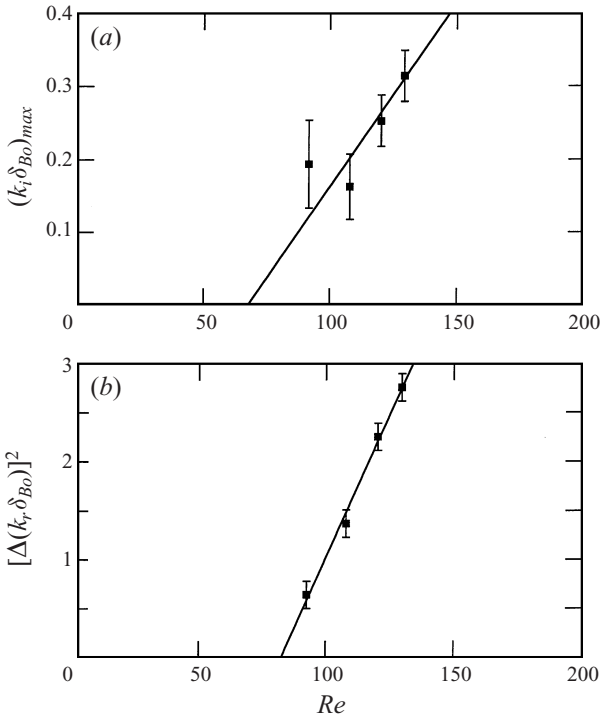

FIGURE 14. (*a*) Maximum of the normalized spatial growth rate $k_i\delta_{Bo}$ as a function of the Reynolds number Re. (*b*) Square of the width of the unstable wavenumber range $[\Delta(k_r\delta_{Bo})]^2$ versus Re.

$[\Omega_0,10\Omega_0]$. As the amplitude of this natural noise is 1/100 of the amplitude of the smallest forcing, the light modulation, being proportional, should be 100 times smaller when $Re < 110$, and as shown by figure 15(*a*), could not be visualized. It is only at larger Re ($Re > 110$) that the amplitude is large enough that the instability is visually detected. This strong influence of the noise level explains why, as already mentioned in § 2, we found visually $Re_c \approx 70$ without adding any forcing to a less well-regulated previous motor. The behaviour of the light intensity above $Re = 110$ (figure 15) will be discussed in § 6.1.

5.5. *Discussion of the most unstable frequency*

We have already seen in figure 10(*b*) that the instability is a large-band noise amplifier with a most amplified frequency around four times the angular frequency of the rotating disk. Such behaviour is confirmed when adding a white noise to the angular rotation of the disk: the light intensity spectrum presents a large peak around $4\Omega_0$ with a standard deviation similar to the one of figure 10(*b*). When no external controlled forcing is added, the circular waves are observed under steady conditions at larger Re ($Re > 110$) but in that case with a frequency exactly equal to $4\Omega_0$ (figure 16). This may be due to the selective amplification by the bell shaped curve of figure 10(*b*) of the harmonics of Ω_0 observed in the signal of the motor. In figure 17, we compare the most unstable frequency ω_{max} observed with and without forcing for various Re. With forcing, the ratio ω_{max}/Ω_0 evolves slightly with Re around the value 4 but is clearly locked to 4 without forcing. In their experimental study, Schouveiler *et al.* (1999) found without controlled forcing a natural frequency of circles that evolves discontinuously along the radius from $3\Omega_0$ at the periphery, through $2\Omega_0$ and finally

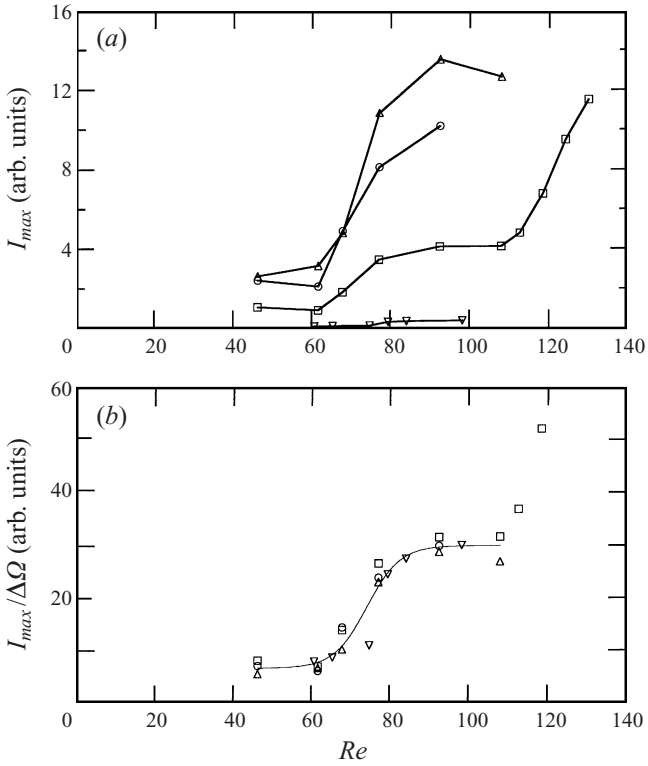

FIGURE 15. (*a*) Maximum light intensity I_{max} at $\omega = 15\,\mathrm{rad\,s^{-1}}$ as a function of the Reynolds number Re for different forcing amplitudes with the same seeded fluid: $\Delta\Omega = 0.47$ (△), 0.34 (○), 0.13 (□), and 0.013 (▽) rad $\mathrm{s^{-1}}$. (*b*) Normalized intensity $I_{max}/\Delta\Omega$ versus Re. The continuous line is a guide for the eye.

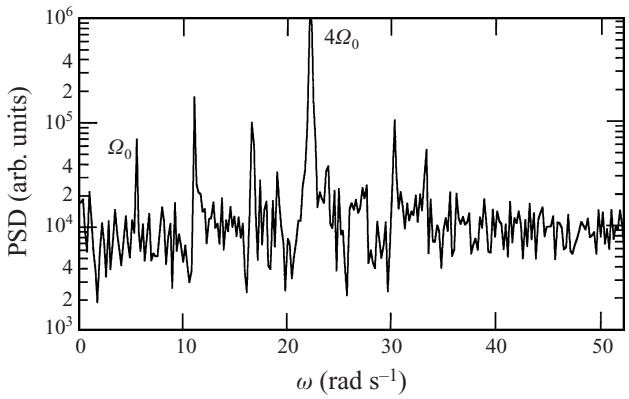

FIGURE 16. Power spectrum density (PSD) of the time signal of the light intensity at $Re = 128$ ($\Omega_0 = 5.42\,\mathrm{rad\,s^{-1}}$) without external controlled forcing.

Ω_0 toward the centre, these changes of frequency being due to pairing of vortices. Similar pairing from $3\Omega_0$ to Ω_0 has been observed numerically for larger aspect ratio by Cousin-Rittemard (1996). In the present study, we did not observe such pairing of the structures, neither with nor without forcing. Note that in the case of a fluid rotating at Ω over a single stationary and infinite disk, Lingwood (1997) found

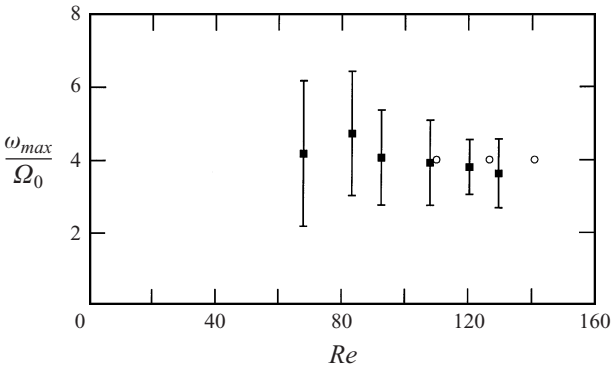

FIGURE 17. Ratio ω_{max}/Ω_0 of the resonant wave frequency to the disk frequency as a function of the Reynolds number Re: forced case (■) and natural case (○). The standard deviations of Gaussian curves like the one of figure 10(*b*) are indicated.

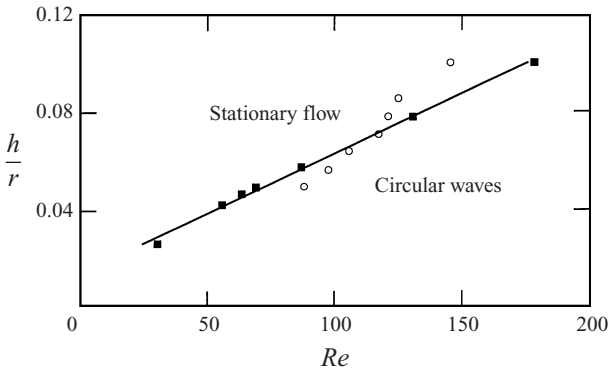

FIGURE 18. Critical Reynolds number Re_c for circle appearance with forcing as a function of the inverse of the aspect ratio $1/\Gamma = h/R$: our results (■) with a linear fit (—) of $Re_c = 29 + 2051/\Gamma$ and results of Schouveiler (1998) (○).

theoretically $\omega/\Omega \approx 1.3$ at the convective/absolute transition for the axisymmetric structures in the Bödewadt layer.

5.6. *Aspect ratio dependence of the threshold*

By varying the height of the cell, we have also studied the influence of the aspect ratio on the threshold of the instability in the presence of noise. The determination of Re_c was here only visual, but this gives a good estimate in agreement with all the determinations presented above. The critical Reynolds number Re_c is plotted versus the inverse of the aspect ratio $1/\Gamma = h/R$ in figure 18. The threshold decreases almost linearly when h decreases and we do not observe any asymptotic value of Re_c for small h. This shows that, at least for $\Gamma < 40$, the threshold of the instability is still dependent on the aspect ratio and thus that the basic profile is still evolving. Thus the flow does not reach an asymptotic regime such as the one described by Brady & Durlofsky (1987). Whatever the choice for the definition of the Reynolds number, the onset depends both on Re and on the aspect ratio Γ and thus cannot be described by a single parameter. Our results are in fair agreement with those recently found by Schouveiler (1998) in a similar cell although he had no controlled forcing in his system. However, he did not observe any circles for $\Gamma > 20$. The numerical results

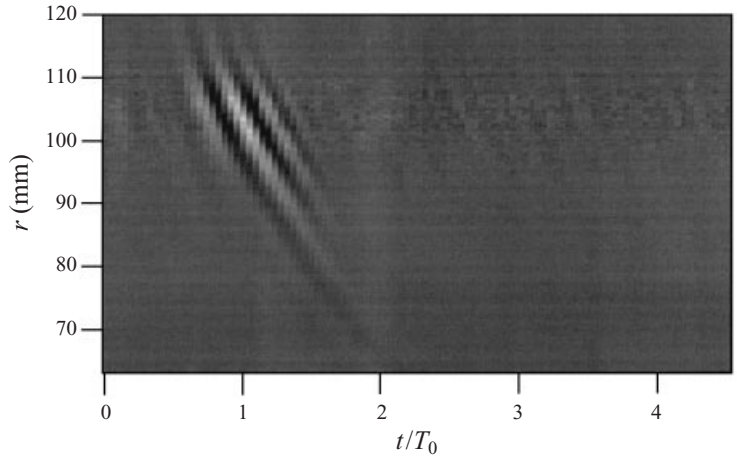

FIGURE 19. Spatiotemporal image of the response to a pulse in Ω_0 at $Re = 108$.

of Cousin-Rittemard *et al.* (1998) also show a similar dependence of the critical Reynolds number on the aspect ratio but their values of Re_c are much larger than the experimental ones (e.g. $Re_c = 900$ instead of 180 for $\Gamma = 10$, which is the largest aspect ratio tested numerically but the smallest one tested experimentally).

6. Flow response to transients

With a periodic forcing of the rotating disk, we have determined the threshold of the instability and its characteristics. We now report the results of some additional experiments where we investigate the flow response to transients in the disk velocity. First, the response to a small impulse or step allows us to test the convective or absolute nature of the instability. Secondly, we have done spin-down to rest experiments in order to compare our results with those of Savas (1983, 1987) and Lopez & Weidman (1996), and thus to determine if the circular waves we observed under steady conditions are of the same kind than those observed in the spin-down experiments.

6.1. *Response to a small impulse: test of a convective or absolute regime*

By studying the response of the flow over a single rotating disk to a local perturbation,Wilkinson & Malik (1985) and more recently Lingwood (1996) have demonstrated experimentally the convective nature of the spirals observed in the Ekman layer. In addition, Lingwood (1996) clearly demonstrated a convective/absolute transition for a higher local Reynolds number. For the rotating flow over an infinite stationary disk, Lingwood (1997) found theoretically the existence of a convective/absolute transition for spirals as well as for axisymmetric waves. For the rotor/stator case, the convective behaviour of the circular waves in the Bödewadt layer has also been observed numerically with steps in the angular velocity by Cousin-Rittemard *et al.* (1998) for $Re = 2000$ and $\Gamma = 6$ and by Lopez (1996) for $Re = 10000$ and $\Gamma = 1$. We have also performed similar experiments briefly perturbing the flow. When $Re < 68$ no structures are observed. For $68 < Re < 110$, the perturbation triggers a few circular waves, and the generated wave packet propagates toward the centre and fades away. In the wave packet we typically observe two to four waves with a mean frequency which is again $\omega/\Omega_0 \approx 4$ (figure 19). After the impulse the flow goes back to the

basic stationary state, which demonstrates the convective nature of the instability. For $Re > 110$, the propagating circular waves are always present in the cell, after or before the perturbation. The still open question is whether such permanent structures are noise-sustained or self-sustained. We recall that noise-sustained structures can be found in a convectively unstable system when the noise existing in the set-up is strongly amplified well above threshold (Deissler 1987). Otherwise, self-sustained structures corresponding to a global mode can be observed for an absolutely unstable system (Huerre and Monkewitz 1990). In our experiment, when one looks again at figure 15, there is a strong increase of the light intensity above $Re = 110$, after the first amplification at $Re = 70$ corresponding to the onset of the convectively unstable regime. We think that this second sudden increase at $Re = 110$ cannot be interpreted in terms of the appearance of noise-sustained structures in a still convectively unstable regime and thus may correspond to a convective/absolute transition of the flow. However, to confirm this point, further experiments would be necessary.

6.2. *Response to spin-down to rest*

Experiments corresponding to the spin-down to rest of a cylindrical tank were first described by Savas (1983, 1987). For a cell of aspect ratio $\Gamma = 0.5$, he observed transient circular waves propagating in the Bödewadt layer when the local Reynolds number r/δ_0 ranges from 25 to 125. The dimensionless wavenumber $k_r\delta_0$ of the structure evolves from 0.6 to 0.2, and the frequency ω seems to scale as $4\Omega_0$ or $5\Omega_0$ (figure 8 of Savas 1987). These scalings of ω and k_r are thus similar to ours made under steady conditions, suggesting that we are observing the same instability. To confirm this point we did spin-down experiments with an aspect ratio of 20.9, starting from the usual steady condition where only the upper disk is rotating. Typically 1 s after stopping the disk we also observe a few bright circular waves propagating inward, but they do not propagate as far as in the periodic forcing experiments. Note that the motion is only observed for a few seconds in accordance to the viscous diffusion time estimated using the cell half-thickness ($(h/2)^2/\nu \approx 5$ s). For initial Reynolds numbers Re ranging from 50 to 105 the wavenumber is again $k\delta_0 = 0.5 \pm 0.1$, thus similar to the one obtained under steady conditions. For $Re < 50$, thus for local $r/\delta_0 < 140$, we do not observe any circles. This minimum value of 140 is much larger than the value 25 obtained by Savas (1987) and the value 27.5 obtained numerically by Lopez & Weidman (1996). This difference is however not surprising when one considers the large difference in aspect ratios. The present minimum value to observe circles $Re = 50$ is smaller than the critical Reynolds number determined in steady conditions ($Re_c \approx 75$). However in this range $50 < Re < 75$, circular waves are generated at the periphery by the strong perturbation induced by the spin-down condition but are damped all along their motion, suggesting that we are below the threshold of the instability. All these results seem to indicate that the spin-down to rest experiments lead to the same instability of the Bödewadt layer as the one characterized quantitatively in § 5 under steady conditions.

7. Conclusion

In this paper we have investigated experimentally the primary destabilization of the flow between a stationary and a rotating disk when the cell is closed and of rather large aspect ratio. This destabilization occurs in the Bödewadt layer and leads to propagative circular waves, which have been only recently discovered under steady conditions. By controlling the mechanical noise level and frequency we have shown

that the flow is a large-band amplifier with a most-amplified frequency of the order of four times the rotation frequency. By visualization means we measured the thickness of the boundary layers existing close to the disks. As usual, the thickness scales as $(\Omega_0/\nu)^{1/2}$ but we have found that the Bödewadt layer becomes larger at smaller radius, following a linear evolution with r. Such an evolution of the Bödewadt layer means that the radial flow is non-parallel there and thus a local scaling is important to describe the dispersion relation of the instability. From our visualizations, we have extracted the local wavenumber and the spatial growth rate of the instability. We have shown that a unique dispersion relation does indeed exist whatever the forcing frequency and the radial position if the data are scaled by the local thickness δ_{Bo} of the layer. Note that a local Reynolds number like the one used in infinite disk geometry was not able to characterize the onset of the instability. The instability has thus been found to have all the properties of a supercritical bifurcation with a threshold $Re_c \approx 75$ for $\Gamma = 20.9$, and a critical wavenumber $k_c\delta_{Bo} \approx 0.5$. The critical Reynolds number of the instability is found to decrease when the aspect ratio is increased. Our control of the noise level shows that above the critical Reynolds number, the instability is linearly convective. For larger Re the flow seems to become absolutely unstable, thus exhibiting self-sustained structures rather than noise-sustained structures. Finally we have made a comparison with the circular patterns observed in spin-down experiments. The wavenumber, frequency and threshold are not very different and thus this suggests that the instability leading to circular waves has the general properties of a shear instability of the radial velocity profile. The study of the most unstable wavenumber and of the most unstable frequency was done for aspect ratio $\Gamma = 20.9$; it remains to be done for other aspect ratios. In the same way, as this axisymmetric instability is also observed for co-rotating disks or slightly contra-rotating disks, the existence domain of this instability remains to be defined in the plane of the angular velocities of the disks.

We thank G. M. Homsy for enjoyable and fruitful discussions and J.-M. Chomaz for suggesting the use of the WKBJ approximation to deduce the dispersion relation from the experimental measurements. Special thanks to C. Saurine and C. Frénois for their technical assistance. Laboratoire FAST (Fluides, Automatique et Systèmes Thermiques) is associated to CNRS and to Universités Paris VI et XI (UMR 7608).

REFERENCES

Batchelor, G. K. 1951 Note on a class of solutions of the Navier–Stokes equations representing steady rotationally–symmetric flow. *Q. J. Mech. Appl. Maths* **4**, 29–41.

Bödewadt, U. T. 1940 Die Drehströmung über festem Grund. *Z. Angew. Math. Mech.* **20**, 241–253.

Brachet, M.-E. 1990 Géométrie des structures à petite échelle dans le vortex de Taylor-Green. *C. R. Acad. Sci. Paris* II **311**, 775–780.

Brady, J. F. & Durlofsky, L. 1987 On rotating disk flow. *J. Fluid Mech.* **175**, 363–393.

Couder, Y., Douady, S. & Brachet, M.-E. 1991 Direct observation of the intermittency of intense vorticity filaments in turbulence. *Phys. Rev. Lett.* **67**, 983–986.

Cousin-Rittemard, N. 1996 Contribution à l'étude des instabilités des écoulements axisymétriques en cavité inter-disques de type rotor-stator. PhD thesis, Université Paris VI.

Cousin-Rittemard, N., Daube, O. & Le Quéré, P. 1998 Sur la nature de la première bifurcation des écoulements interdisques. *C. R. Acad. Sci. Paris* IIb **326**, 359–366.

Croquette, V. & Williams, H. 1989 Nonlinear waves of the oscillatory instability on finite convective rolls. *Physica* D **37**, 300–314.

Deissler, R. J. 1987 Spatially growing waves, intermittency and convective chaos in an open flow system. *Physica* D **25**, 233–260.

Dijkstra, D. & Heijst, G. J. F. van 1983 The flow between finite rotating disks enclosed by a cylinder. *J. Fluid Mech.* **128**, 123–154.

Ekman, V. W. 1905 On the influence of the Earth's rotation on ocean currents. *Arkiv. Mat. Astr. Fys. Bd* 2 **11**, 1–52.

Faller, A. J. 1963 An experimental study of the laminar Ekman boundary layer. *J. Fluid Mech.* **15**, 560–576.

Faller, A. J. & Kaylor, R. E. 1966 A numerical study of the instability of the laminar Ekman boundary layer. *J. Atmos. Sci.* **23**, 466–480.

Fauve, S., Laroche, C. & Castaing, B. 1993 Pressure fluctuations in swirling turbulent flows. *J. Phys.* II *Paris* **3**, 271.

Gauthier, G. 1998 Etude expérimentale des instabilités de l'écoulement entre deux disques. PhD thesis, Université Paris XI.

Gauthier, G., Gondret, P. & Rabaud, M. 1996 Patterns between rotating disks. *Dynamics Days, July 10-13, Lyon* (unpublished).

Gauthier, G., Gondret, P. & Rabaud, M. 1998 Motions of anisotropic particles: application to visualization of three-dimensional flows. *Phys. Fluids* **10**, 2147–2154.

Gregory, N., Stuart, J. T. & Walker, W. S. 1955 On the stability of three-dimensional boundary layers with application to the flow due to a rotating disc. *Phil. Trans. R. Soc. Lond.* A **248**, 155–199.

Hinch, J. 1991 *Perturbation Methods.* Cambridge University Press.

Huerre, P. & Monkewitz, P. A. 1990 Local and global instabilities in spatially developing flows. *Ann. Rev. Fluid Mech.* **22**, 473–537.

Hoffman, N., Busse, F. H. & Chen, W.-L. 1998 Transitions to complex flows in the Ekman-Couette layer. *J. Fluid Mech.* **366**, 311–332.

Itoh, M. 1984 Stability calculations of three-dimensional boundary layer on a rotating disk. In *Laminar-Turbulent Transition* (ed. V. R. Kozlov), pp. 463–470. Springer.

Jarre, S., Le Gal, P. & Chauve, M. P. 1991 Experimental analysis of the instability of the boundary layer over a rotating disk. *Europhys. Lett.* **14**, 649–654.

Jarre, S., Le Gal, P. & Chauve, M. P. 1996*a* Experimental study of rotating disk instability. I. Natural flow. *Phys. Fluids* **8**, 496–508.

Jarre, S., Le Gal, P. & Chauve, M. P. 1996*b* Experimental study of rotating disk instability. II. Forced flow. *Phys. Fluids* **8**, 2985–2994.

Kármán, T. von 1921 Laminar und turbulente reibung. *Z. Angew. Math.* **1**, 233–252.

Lingwood, R. J. 1995 Absolute instability of the boundary layer on a rotating disk. *J. Fluid Mech.* **299**, 17–33.

Lingwood, R. J. 1996 An experimental study of absolute instability of the rotating-disk boundary layer flow. *J. Fluid Mech.* **314**, 373–405.

Lingwood, R. J. 1997 Absolute instability of the Ekman layer and related rotating flows. *J. Fluid Mech.* **331**, 405–428.

Lopez, J. M. 1996 Flow between a stationary and a rotating disk shrouded by a co-rotating cylinder. *Phys. Fluids* **8**, 2605–2613.

Lopez, J. M. 1998 Characteristics of endwall and sidewall boundary layers in a rotating cylinder with a differentially rotating endwall. *J. Fluid Mech.* **359**, 49–79.

Lopez, J. M. & Weidman, P. D. 1996 Stability of stationary endwall boundary layers during spin-down. *J. Fluid Mech.* **326**, 373–398.

Randriamampianina, A., Elena, L., Fontaine, J.-P. & Schiestel, R. 1997 Numerical prediction of laminar, transitional and turbulent flows in shrouded rotor-stator systems. *Phys. Fluids* **9**, 1696–1713.

San'kov, P. I. & Smirnov, E. M. 1984 Bifurcation and transition to turbulence in the gap between rotating and stationary parallel disks. *Fluid Dyn.* **19**, 695–702.

San'kov, P. I. & Smirnov, E. M. 1991 Stability of viscous flow between rotating and stationary disks. *Fluid Dyn.* **26**, 857–864.

Savas, Ö. 1983 Circular waves on a stationary disk in rotating flow. *Phys. Fluids* **26**, 3445–3448.

Savas, Ö. 1987 Stability of Bödewadt flow *J. Fluid Mech.* **183**, 77–94.

Schouveiler, L. 1998 Sur les instabilités des écoulements entre un disque fixe et un disque en rotation. PhD thesis, Université Aix-Marseille II.

Schouveiler, L., Le Gal, P. & Chauve , M.-P. 1998 Stability of a travelling roll system in a rotating disk flow. *Phys. Fluids* **10**, 2695–2697.

Schouveiler, L., Le Gal, P., Chauve, M.-P. & Takeda, Y. 1996 Experimental study of the stability of the flow between a rotating and stationary disk. In *Advances in Turbulence VI* (ed. S. Gavrilakis, L. Machiels & P. A. Monkewitz), pp. 385–388. Kluwer.

Schouveiler, L., Le Gal, P., Chauve, M.-P. & Takeda, Y. 1999 Spirals and circular waves in the flow between a rotating and stationary disk. *Exps. Fluids* **26**, 179–187.

Sirivat, A. 1991 Stability experiment of flow between a stationary and a rotating disk. *Phys. Fluids* A **3**, 2664–2671.

Stewartson, K. 1953 On the flow between two rotating coaxial disks. *Proc. Camb. Phil. Soc.* **49**, 333–341.

Szeri, A. Z., Giron, A., Schneider, S. J. & Kaufman, H. N. 1983 Flow between rotating disks. Part 2. Stability. *J. Fluid Mech.* **134**, 133–154.

Wilkinson, S. P. & Malik, M. R. 1985 Stability experiments in the flow over a rotating disk. *AIAA J.* **23**, 588–595.

Zandbergen, P. J. & Dijkstra, D. 1987 Von Kármán swirling flows. *Ann. Rev. Fluid Mech.* **19**, 465–491.